



From γ -alumina to supported platinum nanoclusters in reforming conditions: 10 years of DFT modeling and beyond



Pascal Raybaud^{a,*}, Céline Chizallet^a, Christophe Mager-Maury^{a,b}, Mathieu Digne^a, Hervé Toulhoat^c, Philippe Sautet^b

^a IFP Energies nouvelles, Direction Catalyse et Séparation, Rond-point de l'échangeur de Solaize, BP3, 69360 Solaize, France

^b Université de Lyon, CNRS, Ecole Normale Supérieure de Lyon, 46 allée d'Italie, 69364 Lyon Cedex 07, France

^c IFP Energies nouvelles, Direction Scientifique, 1 & 4 Avenue de Bois-Préau, 92852 Rueil-Malmaison Cedex, France

ARTICLE INFO

Article history:

Received 6 March 2013

Revised 5 July 2013

Accepted 18 August 2013

Available online 21 September 2013

Keywords:

Alumina
Density functional theory
Platinum
Hydrogenolysis
Reforming
Dehydrogenation
Coking
Ethane

ABSTRACT

Highly dispersed Pt particles on γ -Al₂O₃ are known to catalyze dehydrogenation and hydrogenolysis of alkanes under H₂ pressure which are of main concerns within the context of reforming catalysts. We first highlight recent progresses on the density functional theory (DFT) simulations of γ -Al₂O₃ surfaces, a prerequisite step, and then address the challenging question of γ -Al₂O₃-supported Pt clusters in reactive conditions. For that purpose, we report a DFT study of the thermodynamic stability of C_xH_y (with $x = 1, 2$ and $0 \leq y \leq 5$) species formed upon dissociative adsorption of ethane on Pt₁₃/ γ -Al₂O₃ models at variable H coverages. The impact of the pressure ratio $J = P(\text{H}_2)/P(\text{C}_2\text{H}_6)$ is thus quantified and rationalized as a competition between C_xH_y and H species for cluster sites, combined with cluster morphology effects (reconstruction at high H coverage). We finally discuss these results in detail with the experimental literature.

© 2013 Elsevier Inc. All rights reserved.

1. Introduction

Highly dispersed platinum (Pt) nanoparticles (with sizes in the range 0.8–1 nm) supported on γ -alumina are versatile catalysts widely used in the fields of fine chemistry, petrochemicals, and oil refining. In the latter, one famous application, developed in the 1940s, is the catalytic reforming of naphtha feedstocks into high octane gasoline [1,2]. The major reactions involved in this process are the so-called dehydrocyclization reactions, enabling the conversion of linear alkanes into high octane number aromatic compounds. A side reaction for this process is alkane hydrogenolysis which produces undesired lighter alkanes (including methane). Both reactions have been the subject of numerous experimental works: in particular, it was proposed 50 years ago in Journal of Catalysis that the same sites promote hydrogenolysis, dehydrocyclization, and isomerization of alkane on an alumina-supported platinum catalyst [3]. Later, it was proposed that

dehydrocyclization of hexane for instance is sensitive to Pt particle size and would require low coordination metallic sites most probably located on the corners of Pt particles [4,5]. In particular, platinum particles with sizes in the range 0.8–1 nm when highly dispersed on γ -alumina would provide a local structure exhibiting such low coordination sites.

Within the context of natural gas, it is also worthwhile to underline that the dehydrogenation of alkanes into olefins represent a renewed attraction if we believe more recent publications [6–8]. Pt-based catalysts being able to activate C–H bonds, the dehydrogenation pathways are generally of great interest as they lead to functional alkenes or aromatic molecules starting from linear or cyclic alkanes [1,2]. However, C–C bonds can also be activated by Pt-based catalysts, which may result in unwanted by-products: coke, surface carbide deposited on the active phase, or gas-phase methane. It was proposed that C–C bond scission (through hydrogenolysis) requires a certain degree of dehydrogenation of the alkane molecule [9–13]; hence, it can be intuitively understood that the hydrogenolysis rate will be maximized for the hydrogen pressure $P(\text{H}_2)$ providing a good balance between dehydrogenation steps and the subsequent C–C scission/hydrogenation steps. So, it is often observed that the rate of dehydrocyclization and hydrogenolysis reactions directly depends on the

* Corresponding author. Fax: +33 4 37 70 20 66.

E-mail addresses: pascal.raybaud@ifpen.fr (P. Raybaud), celine.chizallet@ifpen.fr (C. Chizallet), c.magermaury@gmail.com (C. Mager-Maury), mathieu.digne@ifpen.fr (M. Digne), herve.toulhoat@ifpen.fr (H. Toulhoat), philippe.sautet@ens-lyon.fr (P. Sautet).

operating conditions and more specifically on $P(\text{H}_2)$ [12] which is also true for dehydrocyclization reactions involved in naphtha reforming [2,11,14]. In practice, a nonzero partial pressure of H_2 is used in the reactive medium. For instance, for the reforming process using pure platinum as an active phase, the pressure of H_2 may reach 30 bar and $P(\text{H}_2)/P(\text{HC})$ ratio as high as 10, where HC stands for hydrocarbons.

Experimental studies on ideal Pt surfaces have brought significant insights on the nature of C_2H_y and CH_y intermediates likely to be formed upon dissociative adsorption of ethane, ethylene, or acetylene molecules. LEED analysis [15] and microcalorimetric measurements [16] revealed the formation of ethylidyne on Pt(111) adsorbed on a threefold surface site. TPD shows that dehydrogenation of ethane on Pt(110) surface leads to CCH_2 at 350–400 K and CCH at 440 K. Above 540 K, CCH decomposes forming a carbon monolayer [17]. Regarding hydrogenolysis, it appears to be promoted by steps and kinks on platinum surfaces [18] as well as on particles of smaller sizes [19], which strengthens the interest for a deeper understanding of the catalytic behavior of highly dispersed platinum clusters.

Theoretical studies based on density functional theory (DFT) have also dealt with alkane dehydrogenation and hydrogenolysis mechanisms occurring either on infinite surface of platinum [20–22] or on Pt clusters [7,23–25]. Although all these studies brought insights into the energy levels of the possible dehydrogenated intermediates formed along the two pathways, they consider only the cases of zero hydrogen coverage and only one or two co-adsorbed H atoms produced during the dehydrogenation process of the molecule itself. No extra hydrogen atoms brought by the surrounding gas atmosphere was considered to investigate the stability or reactivity of the various intermediates. Actually, very few DFT studies consider the impact of high hydrogen coverage on hydrocarbon adsorption properties. Exceptions are DFT studies of ethylene and acetylene adsorption on Ir_4 cluster [26] and butadiene and butene adsorption on Pd surfaces [27]. According to the aforementioned experimental observations [13], it remains crucial to consider the co-adsorption of the correct amount of hydrogen in order to understand the complex effect of hydrogen on hydrogenolysis and dehydrogenation. Moreover, many theoretical studies did not consider the underlying alumina support although it was recently shown that it modifies the morphology and electronic properties of metallic clusters, such as those found in reforming catalysts [28]. In particular, the morphology of Pt_{13} clusters differs from the gas-phase structure [28,29] and is simultaneously modified by hydrogen coverage as discussed below [30]. So to investigate the elementary steps of C–C and C–H bond scissions, which are sensitive to the coordination number of platinum sites, the morphology effect induced by the support and the reductive environment must be considered carefully.

The goal of the present work is to investigate these challenging questions by using the most advanced models representing platinum particles highly dispersed on γ -alumina. To reach this goal, we used one of the detailed model of the γ -alumina surface first published in Journal of Catalysis as a Priority Communication in 2002 [31] and in a more extended paper 2 years later [32]. Progress made in the DFT simulation of this widely used support was needed prior to addressing complex questions related to the hydrogenolysis and reforming catalysts, scope of the present paper. So within the context of this special issue of Journal of Catalysis, we would like first to recall the progress regarding the simulation of the support and highlight some relevant applications in catalysis published during the last 10 years. We will then come back to the main motivation of the present paper, devoted to highly dispersed platinum (Pt) nanoparticles supported on γ -alumina in reactive environment.

2. $\gamma\text{-Al}_2\text{O}_3$ surfaces: 10 years of DFT modeling applied to catalysis

The starting point of our contribution to a better understanding and prediction of $\gamma\text{-Al}_2\text{O}_3$ surfaces properties in catalysis was the development of realistic surface models sensitive to operating conditions. This initial aim was obtained in two steps: first, the DFT study of boehmite $\gamma\text{-AlOOH}$ transition into $\gamma\text{-Al}_2\text{O}_3$ has been used to determine a reliable $\gamma\text{-Al}_2\text{O}_3$ bulk model [33]. Next, the surface structures inherited from this bulk model were determined for different crystallographic orientations ((100), (110) and (111)) and as a function of the temperature and of the water partial pressure [31,32]. This allows the prediction of the water surface coverage with respect to the pre-treatment operating conditions (such as final calcination temperature at given moisture content). The theoretical determination of the surface energy for the different exposed faces as a function of their hydration state is of a fundamental interest to control the nanoparticles properties, such as size, shape, and surface speciation. Indeed, these characteristics taken together determine the nature and the number of the surface sites (OH groups, coordinatively unsaturated Al surface sites...) and as a consequence the surface catalytic behavior (Brønsted and Lewis acid properties, interactions with reactants and products, deposit and generation of the active phase...). Even if these models can always be improved ($\gamma\text{-Al}_2\text{O}_3$ is mainly an assembly of nanoparticles without long range order therefore appearing as a disordered material), they contain the main features of catalytic $\gamma\text{-Al}_2\text{O}_3$ materials, and DFT simulations are consistent with experimental characterizations: especially, accurate and deep analysis of the spectroscopic Infra-Red data can be achieved by means of these models (OH stretching frequencies assignment, Lewis and Brønsted sites determination using probe molecule adsorption...), leading to important revisions of the pioneering assignment proposed by Knözinger and Ratnasamy [34]. Recently, a microcalorimetry method has been developed to measure the surface energies of $\gamma\text{-Al}_2\text{O}_3$ nanoparticles for different water coverages [35]: a very nice agreement is found with the calculated surface energies, demonstrating that the DFT method can be used to predict the feature of nanoparticles as a function of their size and shape. The two founding papers [31,32] have been cited more than 400 times at the present time, revealing the wide interest of such atomic scale description of $\gamma\text{-Al}_2\text{O}_3$ surfaces in the catalysis community. In what follows, we highlight six relevant – but nonexhaustive – domains in catalysis (including reforming) where these models have been extensively used.

2.1. Alcohol dehydration into ethylene

Recent studies [36,37] have shown that the (100) surface of γ -alumina seems to play a key role for this reaction. Indeed, the control of the hydration state of this face determines to a large extent the alumina reactivity: TPD of ethanol features strongly depend on the alumina pre-treatment prior to ethanol adsorption. For activation temperature lower than 573 K, the TPD peak associated with ethylene formation is found at 523–533 K, whereas this peak moves to 498 K when the activation temperature is higher than 573 K. Indeed, on the basis of the DFT results, the (100) surface becomes fully dehydrated at this temperature, inducing a transition from Brønsted acidic sites (responsible of the peak at 523–533 K) to Lewis acid sites (responsible of the peak at 498 K): the Lewis acid sites are the coordinatively unsaturated Al_v surface sites, specific to the (100) surface. Moreover, for high-temperature activation, a 1-to-1 relation is found between the amount of ethylene molecules and the amount of the pentacoordinated Al_v surface sites that can be either estimated from DFT models or measured by ultrahigh field ^{27}Al NMR [38].

2.2. H_2 , N_2 , and CH_4 activation

Contrary to the (100) surface, the (110) one remains hydrated at elevated temperatures and its Lewis acid sites are not involved in catalytic reactions for medium activation conditions. Nevertheless, when more severe pre-treatment conditions are applied (typically $T > 700$ K and/or $P < 10^{-3}$ Pa), extremely reactive sites are revealed, able to split H_2 and CH_4 molecules [39,40]. Such sites, called “defect sites,” are strongly unsaturated Lewis acid–base pairs, arising from a deep surface dehydration. On the basis of the theoretical model, the Lewis acid sites responsible of such a reactivity has been assigned to the tricoordinated Al_{III} surface sites that are predicted to be specific to the (110) face and become stable at high temperature (they are fully dehydrated for temperature higher than about 1100 K at standard pressure, but they still exist at lower temperature as metastable defect sites or due to the statistical distribution of more or less hydrated zones on the surface, as shown by thermodynamics [39]). This site is able to adsorb N_2 molecule [41], leading to a blue shift of its vibrational frequency (from 2330 to 2355 cm^{-1}). Whatever the reaction (H_2 and CH_4 splitting, N_2 adsorption), the density of these defect sites reaches a maximum at 973 K. At higher temperature, the alumina particles sintering leads to a decrease in surface area and so the concentration of defect sites decreases too.

2.3. Single site catalysis

An example of surface modification leading to complex catalytic systems is the case of single-site heterogeneous catalysis [42] which might be used in olefin metathesis [43], ethylene polymerization [44,45] or arene hydrogenation [46]. In particular, the dehydrated (110) alumina surface has been used to model a supported $Cp_2Zr(CH_3)_2$ catalyst and to compare it to its homogeneous analogue $Cp_2Zr(CH_3)_3^+H_3CB(C_6F_5)_3^-$ [45]. Practically, it has been shown that the geometry (dioxo-bridged or oxo-bridged) and the interaction strength with the basic surface site (μ_3-O or μ_2-O) of the chemisorbed $Cp_2Zr(CH_3)^+$ species strongly impact its reactivity. For ethylene polymerization, the energetics of the π -complex formation is a key point for the global kinetic pathway: the energy of π -complex formation is found to be significantly lower for the $Cp_2Zr(CH_3)^+$ species chemisorbed on μ_3-O site, compared to the μ_2-O case, whereas the formation energy for the homogeneous case stands in-between. This leads to important conclusions in agreement with experimental observations: only a part of the γ - Al_2O_3 -supported single-site metallocene catalysts are catalytically active and they exhibit an activity greater than the homogeneous catalysts.

2.4. Catalytic depollution of automotive exhausts

BaO supported on γ - Al_2O_3 is known to be an efficient catalyst for limiting NO_x emissions from lean-burn engine. This material first stores the NO_x molecules and after reducing period releases it as N_2 and O_2 . A study of the BaO overlayers formation on the γ - Al_2O_3 surface has been proposed [47]: on the dehydrated (100) surface, dispersed BaO species (monomers and dimers) have been found to be thermodynamically stable until a coverage of 4.3 BaO/nm². Beyond this limit, clustering is favored leading to the formation of a structured monolayer on the alumina surface. On contrary, the surface hydration tends to stabilize the BaO monomers and so favors the formations of isolated BaO domains. These DFT results have been confirmed by HR-STEM images [48]: for materials with 2 wt% BaO loading, monomeric BaO unit (anchored to Al_V surface sites) is observed on the (100) surface, where the other surfaces are free of BaO species.

2.5. Hydrotreatment and hydrocracking

γ - Al_2O_3 surface models have been used to generate realistic structures of the amorphous aluminosilicate (ASA) material, especially used for hydrocracking applications [49]. An atomic-scale description of the various Brønsted acid sites present on ASA surface was given. In particular, the peculiar chemical properties of silanols in close vicinity of aluminum atoms (pseudo-bridging silanols) have been highlighted [50–52]. Supported transition metal sulfides nanoparticles have also been modeled with an explicit description of their interactions with the support surfaces and for different hydration state, in a similar way as proposed in other works dealing with metallic nanoparticles [53,54].

2.6. Reforming

Coming back to the application of reforming catalysts motivating the present paper, acid properties of the alumina support are finely tuned by chlorination [55], a well-known industrial method to enhance the surface acidity but also metallic dispersion needed for the reforming process [1,2]. The adsorption isotherms of HCl and the relative surface concentration of hydroxyl groups and chlorine species on the γ -alumina surfaces were thus determined as a function of temperature and H_2O and HCl partial pressures [55] and compared to the experimental conditions of reforming. Cl-atom exchange (by replacement of the basic surface OH groups) is strongly dependent on the exposed surface ((100), (110) or (111)) and the acidity of the Brønsted sites in the vicinity of the Cl atoms is enhanced (leading to the formation of a pyridinium ion after pyridine adsorption, in agreement with the experimental observations).

Beyond, we further investigated the key role of chlorine on the size of platinum particles deposited on chlorinated γ -alumina surfaces: it was shown in particular that chlorine helps for the stabilization of small Pt_3 clusters [56]. Moreover, it was shown that the underlying γ -alumina support influences the morphology and local structure of the Pt_{13} clusters: in particular, on the (100) γ - Al_2O_3 surface, the stable morphology is biplanar (BP) [28] which is not the case for unsupported clusters [29]. This result justifies that we consider the support in our simulation when dealing with highly dispersed systems. In addition, we showed that the platinum cluster is very sensitive to hydrogen pressure encountered in the reforming process. The cluster hydrogen coverage might reach H/Pt close to 1 in reforming conditions ($P(H_2)$ around 10 bars, and $T \sim 800$ K) and when it increases above 1.5 H/Pt, a strong reconstruction of the BP structure into a cuboctahedral (CUB) morphology occurs [30]. This reconstruction is associated with a large change in electronic properties: for H/Pt below 1.4 (including reforming conditions), the platinum sites are metallic, whereas for H/Pt above 1.5, they become positively charged hence partially oxidized (H atoms having simultaneously a hydride character). Indirect evidence of such morphology changes (evolution of Pt–Pt distances and coordination numbers) induced by high hydrogen coverage were observed during XAS experiments [57–60]. This is expected to influence the hydrogenolysis and dehydrogenation pathways as illustrated in the present work. The change in morphology associated with the modulation of electronic properties is induced by an intimate effect of hydrogen coverage and metal-support interactions, which offers us an opportunity to revisit historical and empirical concepts underlined in Introduction [1,13] in the field of alkane hydrogenolysis and dehydrogenation by means of density functional theory (DFT) calculations.

To better describe and understand the impact of hydrogen in the dehydrogenation and hydrogenolysis reactions catalyzed by platinum particles, we report here an *ab initio* study of the thermodynamic stability of C_xH_y ($x = 1$ or 2 and $0 \leq y \leq 5$) intermediates

likely formed upon activation of ethane on supported Pt₁₃ clusters at variable hydrogen coverage θ_{H} .

The present work will thus analyze the effect of the support on the morphology as well as the impact of reaction conditions on the stability of carbonaceous species on Pt nanoclusters. By reaction conditions we mean the influence of temperature and of pressure ratio $P(\text{H}_2)/P(\text{C}_2\text{H}_6)$ on the thermodynamics of the system. In line with our previous works [28,30], we focus on Pt₁₃ clusters as their size is representative of real particle sizes of reforming catalysts (diameter near 0.9 nm), supported on the dehydrated and dechlorinated (100) alumina surface. Even if this surface orientation represents 20% on the surface exposed by the alumina platelets, strong metal–support interaction exists there [28,30,56] so that we chose this surface first. The role of surface adsorbates (chlorine, hydroxyls) present on the alumina (110) surface will be the subject of future studies.

3. Methods

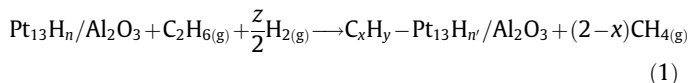
3.1. Total energy calculations

Periodic DFT calculations were carried out with the PW91 exchange–correlation functional [61] as implemented in VASP 4.6 [62,63]. The projected augmented wave (PAW) method [64] was used to describe the core–electron interactions and the plane wave basis set was limited to kinetic cut-off energy of 400 eV. Partial occupancies were determined thanks to a Gaussian smearing with a width of 0.02 eV. Systems were modeled with a $16.71 \times 16.78 \text{ \AA}^2$ surface cell of dehydrated (100) γ -alumina surface which consists in four alumina layers separated by a vacuum thickness of about 15.4 Å. Energies were calculated at the Γ point, and a dipolar correction following the axis perpendicular to the surface was applied due to the adsorption of the platinum clusters only on one-side of the alumina slab. Structures were optimized until the forces were lower than 0.05 eV \AA^{-1} .

3.2. Thermodynamic model

Calculations of the Gibbs reaction energy $\Delta_r G$ were performed to describe the relative stability of adsorbed C_xH_y entities (Eq. (1)) at 800 K (typical of reforming reaction conditions [1,2]), as a function of $J = P(\text{H}_2)/P(\text{C}_2\text{H}_6)$ and $P_r = P(\text{H}_2) + P(\text{C}_2\text{H}_6)$. The reference is the system without any intermediate adsorbed Pt₁₃H_n/Al₂O₃, where n , the number of hydrogen atoms adsorbed initially, is determined by the temperature and H₂ partial pressure according to our previous study [30] as illustrated in Fig. 1. As explained below, n will be optimized in presence of co-adsorbed carbonaceous species.

The Gibbs energy of reaction $\Delta_r G$ refers to Eq. (1) where the transformation of the ethane molecule leads to various C_xH_y carbonaceous species. For each J value, the θ_{H} value was adjusted around the values shown in Fig. 1 according to the presence of C_xH_y , to obtain the optimal state (lowest $\Delta_r G$).



with $n' = n + z - 2(1-2x) - y$. Note that z can either be positive or negative, depending on initial cluster coverage, adsorption mode of C_xH_y , morphology change, and H consumption for methane production.

Chemical potentials μ for all gaseous species involved in the reaction (H_2 , CH_4 , C_2H_6) were calculated according to the ideal gas model, partition functions for rotational and translational terms being estimated thanks to the analysis performed with the

DMol³ code (using the GGA-PW91 functional and a TNP basis set) [65]. We neglect the change in vibrational contributions upon adsorption. These calculations were made for $P(\text{H}_2)$ and $P(\text{C}_2\text{H}_6)$ values reported in Table 1.

For the estimation of $P(\text{CH}_4)$, we assumed that the thermodynamic equilibrium is reached for the reaction depicted by Eq. (2), leading to Eq. (3).



$$P_{\text{CH}_4} = P^0 \exp \left(\frac{1}{2RT} [\mu_{\text{H}_2}^0 + \mu_{\text{C}_2\text{H}_6}^0 - 2\mu_{\text{CH}_4}^0] + \ln \frac{P_{\text{C}_2\text{H}_6}}{P^0} + \ln \frac{P_{\text{H}_2}}{P^0} \right) \quad (3)$$

$\mu_{\text{H}_2}^0$, $\mu_{\text{C}_2\text{H}_6}^0$ and $\mu_{\text{CH}_4}^0$ are the standard chemical potentials of hydrogen, ethane, and methane, respectively. Under these conditions, it can be demonstrated that the Gibbs free enthalpy of the reaction (1) can be expressed as follows (see also Supplementary materials S1):

$$\Delta_r G = \Delta_{\text{ads}} U + \Delta h^0 + \frac{1}{2} [t\mu_{\text{H}_2}^0 - x\mu_{\text{C}_2\text{H}_6}^0] + \frac{RT}{2} \left[x \ln J + (t-x) \ln \left(\frac{JP_r}{J+1} \right) \right] \quad (4)$$

where

$$\Delta_{\text{ads}} U = U_{\text{C}_x\text{H}_y - \text{Pt}_{13}\text{H}_n/\text{Al}_2\text{O}_3} + (2-x)U_{\text{CH}_4} - U_{\text{Pt}_{13}\text{H}_n/\text{Al}_2\text{O}_3} - U_{\text{C}_2\text{H}_6} - \frac{z}{2}U_{\text{H}_2} \quad (5)$$

is the reaction energy relative to Eq. (1), and with:

$$\Delta h^0 = h_{\text{C}_2\text{H}_6}^{\text{OK}} + \frac{z}{2}h_{\text{H}_2}^{\text{OK}} - (2-x)h_{\text{CH}_4}^{\text{OK}} \quad (6)$$

h_i^{OK} being the molar enthalpy of the i gaseous species at 0 K, and with :

$$t = 2 - x - z \quad (7)$$

The chemical potentials of condensed phases were supposed to be independent of adsorbate coverage. Note that we neglected the entropy and thermal variation of the condensed phases. Although this may be at the origin of an underestimation of the stability of the adsorbed HC species, these terms are suspected to vary slightly along the reaction pathway because all intermediates are of small sizes (C1 and C2) with strong Metal–Carbon chemical bonding. For H₂ molecules dissociated on Pt₁₃ upon adsorption, we assume that the vibrational contribution in the adsorbed state can be neglected. As for hydrocarbons, we assume that there is neither rotational nor translational entropy for H atoms in their adsorbed states, while they are considered for molecular H₂ in gas phase. We cannot exclude that entropy effects related to translational motion of H atoms may take place on the Pt cluster at 800 K. If one excepts $J = 0.01$, the high surface density of co-adsorbed species (H, C_xH_y) induces sterical constraints to the translational motion. Moreover, due to the small and finite size of the Pt particles and the strong bonding character of H atoms on the low coordination sites of the cluster, a 2D ideal gas model cannot be applied, so we decided to neglect translation entropy as it was done in Ref. [30].

4. Results

4.1. Clusters morphology and initial H content

We considered a temperature of 800 K and a H₂ partial pressure of 0.2, 10, 18.2, and 99 bar (desired reaction conditions as described earlier, see Table 1). Our previous work [30] has predicted a H coverage of 4 H atoms per Pt₁₃ cluster for $J = 0.01$, 18 for both $J = 1$ and $J = 10$, and 26 for $J = 100$, in the absence of hydrocarbon. The clusters with 4 and 18 H atoms exhibit a biplanar-like (BP)

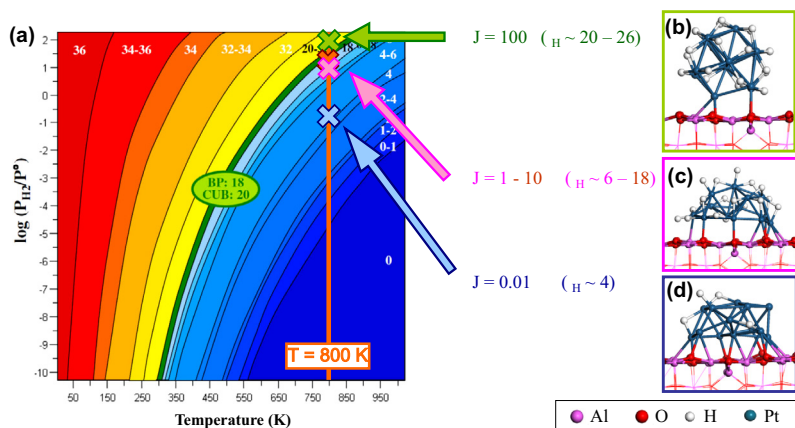


Fig. 1. (a) Thermodynamic diagram depicting the hydrogen coverage on supported Pt_{13} clusters as a function of $P(\text{H}_2)$. Operating conditions considered for the interaction with hydrocarbons are shown and the stable hydrogenated particles depicted in (b) 20 hydrogen atoms, (c) 18 hydrogen atoms, (d) 4 hydrogen atoms. (adapted from Ref. [30]). J stands for the $P(\text{H}_2)/P(\text{C}_2\text{H}_6)$ ratio. The number of H atoms per cluster is reported on each colored region of the diagram.

Table 1

Sum of H_2 and C_2H_6 partial pressures (P_T) and their corresponding partial pressures (in bar) involved in the four reaction conditions with various $J = P(\text{H}_2)/P(\text{C}_2\text{H}_6)$ considered in the present work.

	$J = 0.01$	$J = 1$	$J = 10$	$J = 100$
P_T	20	20	20	100
$P(\text{H}_2)$	0.2	10	18.2	99
$P(\text{C}_2\text{H}_6)$	19.8	10	1.8	1

morphology, whereas the cluster with 26 H atoms exhibits a cuboctahedral shape (CUB) (Fig. 1), according to the morphology transition induced by the 20 H atoms adsorbed on the cluster as described in Ref. [30]. In the presence of adsorbed hydrocarbons, the H coverage and morphology are expected to fluctuate around these critical values as a function of the nature of the C_xH_y intermediates. Hence, the H coverage together with the morphology needs to be optimized along the reaction pathway. Regarding hydrogen adsorption, in the absence of hydrocarbons, the position of the various H atoms was investigated by molecular dynamics, as explained in Ref. [30]. On these H pre-covered clusters, the hydrocarbon adsorption site was sampled systematically on the various positions allowed by the cluster geometry. We only consider the case when one ethane molecule is transformed on the cluster. The optimal systems correspond to the lowest $\Delta_r G$ values for the sampled configurations in each set of reaction conditions. Note that we provide the results for the most stable conformations, although the position of the intermediates on the clusters may change along the reaction scheme. We hence assume that diffusion and reconstruction barriers are small and that diffusion on the cluster is not a rate limiting step.

The bare Pt cluster ($\theta_{\text{H}} = 0$) was considered initially: for the sake of clarity, the corresponding structural results and $\Delta_{\text{ads}}U$ analysis are reported in the Supporting materials S2. In the following, only $\Delta_r G$ values calculated for the optimal coverage of species are reported graphically in the manuscript, all numerical values being explicitly given in the Supporting materials S3.

4.2. “Symmetric” dehydrogenation pathway: toward ethylene and acetylene

The symmetric dehydrogenation reaction of ethane consists in the monodehydrogenation of the two C atoms alternatively. The

successive adsorbed intermediates are ethyl (H_3CCH_2), ethylene (H_2CCH_2), vinyl (H_2CCH), acetylene (HCCH) and ethynyl (HCC), as illustrated in Fig. 2a. Note that we did not consider the molecular (nondissociative) adsorption of ethane on the cluster, which is mainly driven by dispersion interactions that are poorly taken into account by DFT with GGA functionals.

The dehydrogenation steps of ethane to ethyl and ethylene are energetically favored on the bare cluster with the BP morphology as highlighted by the $\Delta_{\text{ads}}U$ profile reported in the Supporting materials S2.1. When referenced to ethylene in the gas phase and to a Pt_{13} cluster holding two H atoms, the adsorption energy of ethylene in a di- σ mode is -153 kJ mol^{-1} , more exothermic than reference results evaluated between -99 to -127 kJ mol^{-1} on the extended $\text{Pt}(111)$ surface for the same adsorption mode (some of them with similar methodology: PW91 functional and plane wave basis set) [22,66–72]. This suggests that there is either a size or a support effect. Microcalorimetric measurements report heat of ethylene adsorption of -120 kJ mol^{-1} at 173 K on Pt powder [72], conditions for which di- σ bonded ethylene is predominant on the surface. DFT calculations on Pt_{10} [24] (using B3LYP functional and local basis set) reported values of -149 kJ mol^{-1} , and values of -133 kJ mol^{-1} and -113 kJ mol^{-1} for Pt_{19} and Pt_{38} clusters [73] (using PW91 functional and a plane wave basis set), for the adsorption of gas-phase ethylene, in good agreement with our results. For acetylene, we calculated an adsorption energy of -247 kJ mol^{-1} , being more exothermic than on the $\text{Pt}(111)$ surface, evaluated at -218 kJ mol^{-1} [66]. The higher stabilization on clusters than on the extended (111) surface is thus assigned to the size effect, due to the well-known higher reactivity of low coordinated metal atoms [73–75].

Upon inclusion of the variations of H contents and the contribution of the entropy of gaseous species, $\Delta_r G$ profiles are shifted to positive values, due to the entropy loss of ethane upon adsorption (Fig. 2d) at the high reaction temperature of 800 K. Adsorbed ethylene represents a local $\Delta_r G$ minimum along the pathway, whatever the J value. Further dehydrogenation is disfavored from a thermodynamic point of view. All intermediates are more stable in hydrogen poor conditions, as shown by the evolution of the $\Delta_r G$ profile as J increases. As expected from chemical intuition, strongly dehydrogenated intermediates are disfavored at higher H_2 pressures, so that a competing adsorption effect occurs between hydrocarbons and H_2 . Generally, co-adsorption of carbonaceous species and hydrogen also tends to decrease the H coverage for

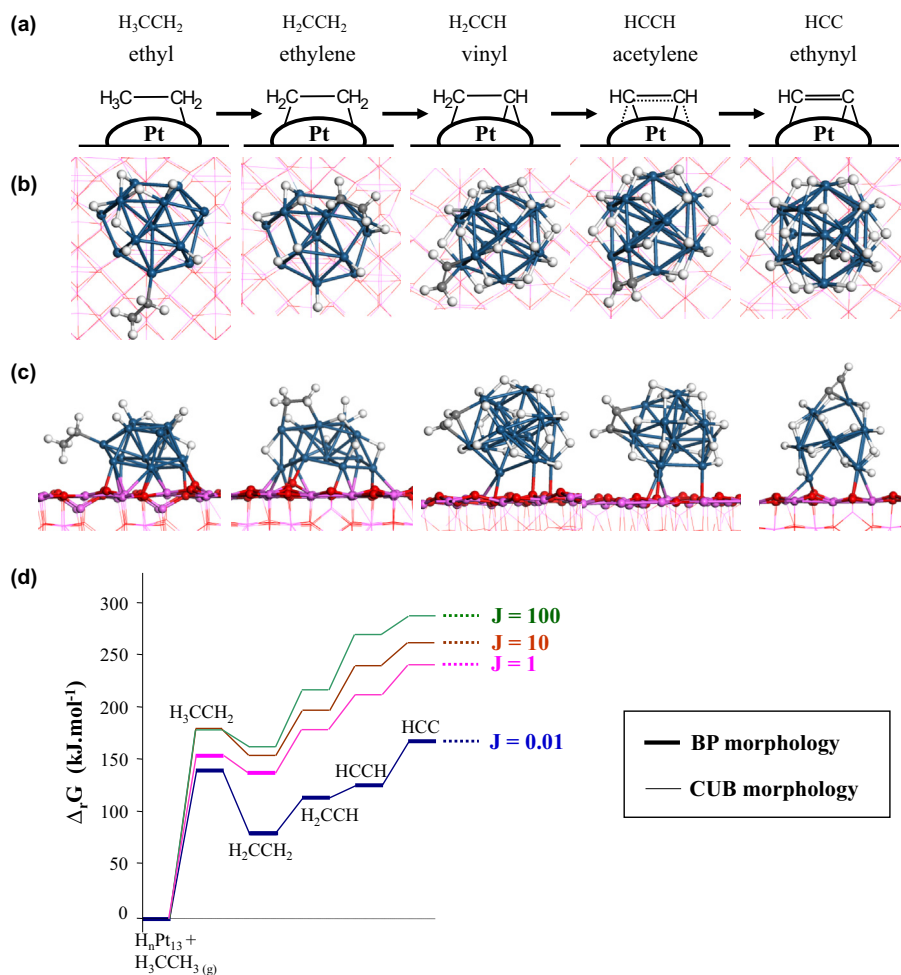


Fig. 2. Symmetric dehydrogenation pathway: (a) Scheme of the intermediates involved, (b) top and (c) side views of the optimal intermediates, taking into account hydrogen coverage, for $J = 1$. Note that a BP to CUB reconstruction may occur along the pathway depending on the J value. (d) $\Delta_r G$ diagram.

the most stable C_2H_y adsorbed on the Pt_{13} cluster (see θ_H values reported in the [Supporting materials S3](#)), due to the fact that the C_2H_y moieties (except ethyl) occupy several coordination sites. This is another illustration of the competition between hydrocarbons and H for the adsorption site on the cluster.

Whatever the J value, ethylene is always adsorbed according to a di- σ mode. Accordingly, all other intermediates exhibit only tetra-valent carbon atoms on the cluster, with two exceptions: acetylene and ethynyl. Acetylene, at low H coverage, adopts a di- σ adsorption mode bridging two Pt atoms (see [Supporting materials S2.2](#)) but switches to a 3-fold hollow site on the CUB morphology for $J = 1, 10$ and 100 , as usually found on extended $Pt(111)$. The ethynyl species follows a similar trend with a strong impact of the CUB morphology on its adsorption mode at $J = 1$ and above.

For $J = 100$, the CUB morphology remains stable along the full pathway. All other operating conditions promote the BP morphology for adsorbed ethylene. At $J = 0.01$, the BP morphology is the most stable one along the whole pathway, whereas for $J = 1$ (Fig. 2b and c) and 10 , a morphology change during the dehydrogenation of ethylene into vinyl in particular. Indeed, during dehydrogenation, the particle must accommodate a higher number of hydrogen atoms: the CUB morphology allows this better than the BP one. As underlined in Section 2, such high hydrogen coverage have already been inferred under pure H_2 atmosphere by XAS experiments [57–59] and DFT calculations [30,60]. Our calculations highlight that such high coverage on platinum clusters may also exist under (HC, H_2) reactive medium.

4.3. “Dissymmetric” dehydrogenation pathway: the ethylidyne trap

The dissymmetric dehydrogenation reaction leads to the complete dehydrogenation of the first C atom followed by the dehydrogenation of the second one. The intermediates involved along this reaction path are the following: ethyl (H_3CCH_2), ethylidene (H_3CCH), ethylidyne (H_3CC), vinylidene (H_2CC), and ethynyl (HCC) (Fig. 3a).

The first three dehydrogenation steps of ethane leading to ethylidyne are energetically favored on the basis of $\Delta_{ads}U$ analysis reported in the [Supporting materials S2.2](#). Surface science techniques such as LEED, RAIRS, and microcalorimetry have revealed the existence of the alkylidyne intermediate on $Pt(111)$ surface [15,16,76]. This result was also observed for silica-supported platinum systems [77]. Microcalorimetric values for the dissociative ethylene adsorption are enclosed between -174 and -150 $kJ\ mol^{-1}$ [16,77–79]. In addition, DFT calculations on the $Pt(111)$ -extended surface found ethylidyne as a highly stable intermediate [20,22,24,25,72,80,81] and $\Delta_{ads}U$ values referenced to gas-phase ethylene including H atoms adsorbed on the bare surface vary from -139 to -155 $kJ\ mol^{-1}$. These values are slightly less negative than ours on the supported cluster (-178 $kJ\ mol^{-1}$) which might be attributed to size and coverage effects.

When entropy effects are included, the reaction pathway becomes endergonic ($\Delta_r G > 0$) as for the symmetric dissociation pathway. However, for J from 0.01 to 10 , ethylidyne stands for a $\Delta_r G$ minimum (as for the $\Delta_{ads}U$ analysis). By contrast with ethylene

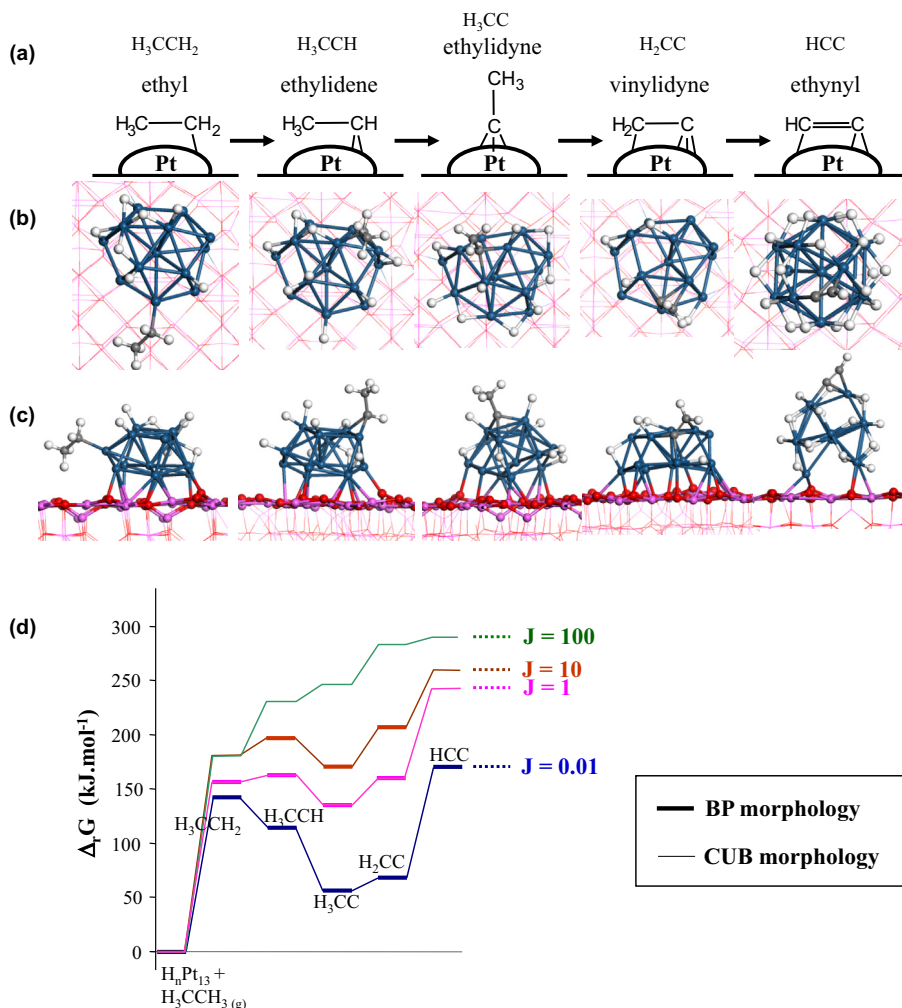


Fig. 3. Asymmetric dehydrogenation pathway: (a) Scheme of the intermediates involved, (b) top and (c) side views of the optimal intermediates, taking into account hydrogen coverage, for $J = 1$. Note that a BP to CUB reconstruction occurs along the pathway. (d) $\Delta_r G$ diagram.

and acetylene, this compound cannot directly desorb from the particle. It is thus expected to be a dormant species on the catalyst. In particular for low $J = 0.01$, it is the most favorably adsorbed carbonaceous species modeled so far, as experimentally observed [15,16,76,77]. Interestingly, Fig. 3 shows also that H_2CC is rather close in energy to H_3CC which is coherent with the observation of H_2CC during ethane dehydrogenation on Pt(110) surface at 350–400 K in the absence of H [17].

Increasing J destabilizes all species, as previously observed for the symmetric dehydrogenation pathway, but also strongly affects the shape of the $\Delta_r G$ profile. Ethylidyne is strongly destabilized at higher J values, as a consequence of the need of three available Pt adsorption sites (Fig. 3a–c). This configuration is hardly obtained in a hydrogen-rich atmosphere: high H coverage blocks adsorption sites needed for the ethylidyne species. A consequence of this is the loss of trapped character (according to the relative stability of the intermediates) for ethylidyne at $J = 100$. Thus, the formation of ethylidyne is prevented by the thermodynamic profile along the path under high excess of hydrogen.

Contrasting with the symmetric dehydrogenation pathway, the BP morphology prevails in a wider set of conditions: only for $J = 100$, the CUB is predominant. If we consider again ethylidyne, it is adsorbed through the C atom in a threefold hollow site involving 3 Pt sites, which hinders the stability of co-adsorbed H atoms ($\theta_H = 9$, for $J = 1$ and 10). Along the symmetric pathway, the vinyl

intermediate interacts with 2 Pt sites which allows a higher number of co-adsorbed H atoms ($\theta_H = 19$, for $J = 1$). As a result, in the symmetric pathway the CUB morphology is favored at $J = 1$ as soon as the vinyl intermediate is formed.

Comparing symmetric and dissymmetric dehydrogenation pathways, once the common ethyl intermediate is formed, the formation of ethylene appears to be clearly in competition with that of ethylidyne. $\Delta_r G$ values of these two key intermediates are compared in Fig. 4: the competition clearly depends on the J ratio. Increasing J destabilizes more rapidly ethylidyne than ethylene. In hydrogen-rich conditions, ethylidyne is thus no longer energetically favored with respect to ethylene formation. Since ethylidyne is located in a potential energy well with respect to acetylene and ethylene (Fig. 4), at low J (0.01), starting from ethylene or from acetylene in the presence of H_2 , ethylidyne is formed as it was observed by LEED, RAIRS, and TPD analysis on Pt(111) surfaces [82,83] and proposed from kinetic modeling on Pt/SiO₂ systems [84]. $J = 1$ appears to be the critical condition at 800 K where both species are equally stable.

At this stage, we also underline that our model gives relevant indication on the thermodynamic trend for the reverse reactions: for instance, hydrogenation of ethylene into ethane. Fig. 2d shows that its rehydrogenation in ethyl becomes much easier by increasing J . In particular, for $J = 10$, ethyl is only 27 kJ/mol higher in energy than ethylene, whereas it was 58 kJ/mol higher at $J = 0.01$.

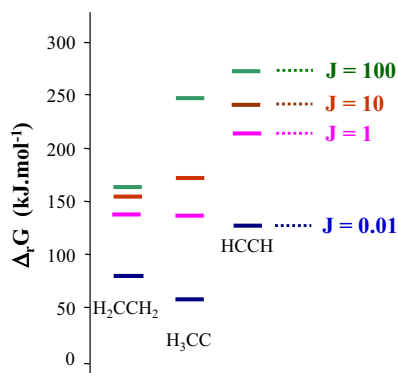


Fig. 4. Comparison of the stability of adsorbed ethylene, ethynylidyne, and acetylene species as a function of operating conditions given by J values.

This trend reveals that there is also a thermodynamic limit in the increase in J with respect to the backwards hydrogenation process.

4.4. C–C bond scission: toward hydrogenolysis, coke, and carbide

Along the dehydrogenation pathways previously studied, the C–C bond breaking leads to the formation of monocarbonaceous CH_x species (Fig. 5a) being either hydrogenated into methane, or dehydrogenated into carbonaceous (CH or C) deposited on the cluster as invoked on infinite platinum surfaces [83]. The highly dehydrogenated CH_x species are expected to be the precursors of coke or surface carbide. Intermediates presented for the symmetric and dissymmetric dehydrogenation pathways can undergo such C–C bond scissions.

In the absence of pre-adsorbed hydrogen, the dissociation of a highly hydrogenated intermediate is generally less favorable than its dehydrogenation (Supporting information S2.3): a C–H bond scission is preferred compared to a C–C bond scission. By contrast, the C–C cleavage of dehydrogenated species H_2CCH and HCC is exoenergetic, whereas all other intermediates (such as H_3CCH and HCCH) show an endoenergetic behavior. However, the formation of HCC is highly endoenergetic, so the preferential intermediate for C–C bond breaking is likely the vinyl species. DFT calculations on a Pt_8 flat cluster [23] are in line with our results for H_2CCH and HCC , but differ for HCCH and H_3CCH for which the C–C scission was predicted to be exothermic. This apparent contradiction can be first due to the different morphology of their Pt_8 cluster (a flat one). Second, the coverage effect in our study may also play a role. Indeed, in [23] only one CH_y was simulated on each cluster. In our case, we decided on purpose to keep the two CH_y fragments on the same cluster in order to take into account lateral interactions in the surface species formed by the C–C bond breaking step. DFT calculations of the energy barriers of the C–C bond cleavage on extended Pt surfaces found a lower activation energy from the HCC intermediate on the flat $\text{Pt}(111)$ and from H_3CCH_2 species on the stepped $\text{Pt}(211)$ surfaces [20]. Other DFT calculations of C–C activation energy on Pt_{10} clusters propose that several C_2H_x intermediates with $x = 2$ –5 may be the precursor states [25]. So, even at low H coverage, there is no consensus on the precursor state for C–C activation which may also be sensitive on the coordination number of active sites involved.

Calculated $\Delta_r G$ values (Table S3 in Supporting materials) for the C–C bond scission are displayed in Fig. 5 for the symmetric and the dissymmetric dehydrogenation paths, at $J = 0.01$. Once a certain stage of dehydrogenation of C_2H_y is reached, the C–C bond scission can occur as the thermodynamically preferred step. From the calculated stability of the respective intermediates, the C–C scissions of vinyl (H_2CCH) (Fig. 5b) and H_2CC (Fig. 5c) are likely to occur,

rather than the subsequent dehydrogenation steps. The scission of H_2CCH into $(\text{CH}_2)(\text{CH})$ is even exergonic at $J = 0.01$. This aspect will be discussed in detail in Section 5.

Further dehydrogenation steps lead to methylidyne and co-adsorbed carbide $(\text{CH})(\text{C})$ that is the most stable dissociated species in these thermodynamic conditions. Observation of methylidyne on $\text{Pt}(111)$ [83] is in line with the metastability ($\Delta_r G > 0$ but local minimum) of the monocarbonaceous CH species in the dehydrogenation of ethane after the C–C bond scission. Note that adsorbed ethylene is not energetically prone to direct dissociation into $(\text{CH}_2)(\text{CH}_2)$, which is the least stable species resulting from a C–C bond breaking in these conditions. By contrast, from a thermodynamic point of view, we cannot rule out the ethane dissociation either directly or through the ethyl species into two methyl species $(\text{CH}_3)(\text{CH}_3)$ which are energetically slightly above the ethyl intermediate. Only kinetic considerations might help to differentiate the two pathways.

Fig. 6 reports some relevant energy profiles for possible C–C bond scission pathways for higher J values. Depending on reaction conditions, various intermediates are likely dissociated along the symmetric and dissymmetric dehydrogenation pathways: H_3CCH_2 , H_2CCH_2 , H_3CCH , H_2CCH , H_2CC , HCC . Red¹ arrows in Fig. 6 indicate some possible reaction energy (not fully exhaustive, for sake of clarity) variations for C–C bond breaking involved when starting from such intermediates. These results will be further discussed in the next section.

As J increases, the global $\Delta_r G$ profile becomes significantly and rapidly more endergonic for highly dehydrogenated monocarbonaceous species than the moderate dehydrogenation of C_2H_y species into ethylene (as it can be seen in Figs. 6, 2d and 3d). This means that the increase in the hydrogen pressure rapidly limits the formation of $(\text{C})(\text{C})$ species which could be considered as coke and/or carbide precursor.

We also report in Fig. 6, $\Delta_r G$ corresponding to methane desorption while keeping a single adsorbed CH_y species ($y = 2$ and 3). The entropy gain due to the release of methane is a stabilizing factor, with respect to clusters with the two adsorbed CH_y species. Since the increase in J destabilizes rapidly the most highly dehydrogenated monocarbonaceous species, hydrogenolysis is suspected to involve H_xCCH_y and $(\text{CH}_x)(\text{CH}_y)$ species with a moderate or low dehydrogenation degree. This aspect will be discussed in the next section.

Regarding the cluster morphology evolution in the presence of monocarbonaceous species, for $J = 0.01$ and 1 it remains mainly BP with two important exceptions for $J = 1$: $(\text{CH}_2)(\text{CH}_2)$ and $(\text{CH}_3)(\text{CH}_2)$. This implies that monocarbonaceous species and particularly the most dehydrogenated ones (highly coordinated with Pt sites) stabilize the BP structure by preventing H adsorption. For $J = 1$, the CUB morphology is stabilized for $(\text{CH}_2)(\text{CH}_2)$ and $(\text{CH}_3)(\text{CH}_2)$ intermediates in presence of a high H coverage (19 and 18 respectively, Supporting materials S3) which may enhance the subsequent formation of methane according to a hydrogenolysis mechanism.

For $J = 100$, the destabilization of $(\text{CH}_3)(\text{C})$, $(\text{CH})(\text{C})$, and $(\text{C})(\text{C})$ species can also be explained by morphology effects. The H coverage of the most stable systems is equal to 9, 5 and 12, respectively (see Supporting materials S3), which are rather low in these thermodynamic conditions. At the same time, the morphology is not a CUB anymore, but rather a BP-type structure. This can be assigned to the presence of (C) atoms, which need to form three to four C–Pt bonds to be stabilized. This is not compatible with a dense CUB morphology, which becomes excessively distorted in the presence

¹ For interpretation of color in Fig. 6, the reader is referred to the web version of this article.

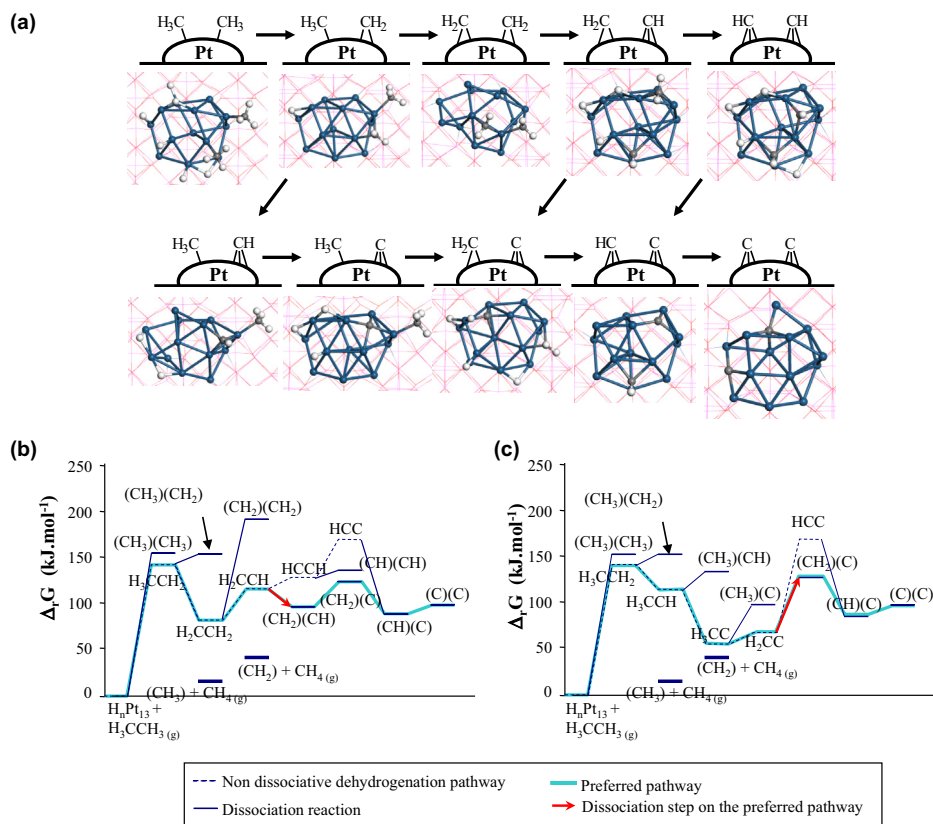


Fig. 5. (a) Intermediates obtained after C–C bond scission. Top views of most stable structures found for $J = 0.01$ are also given. $\Delta_r G$ profile of: (b) symmetric and (c) asymmetric dehydrogenation pathways, including intermediates issued from C–C bond scission, for $J = 0.01$. In parentheses are given the monocarbonaceous species adsorbed on the cluster after the C–C bond breaking.

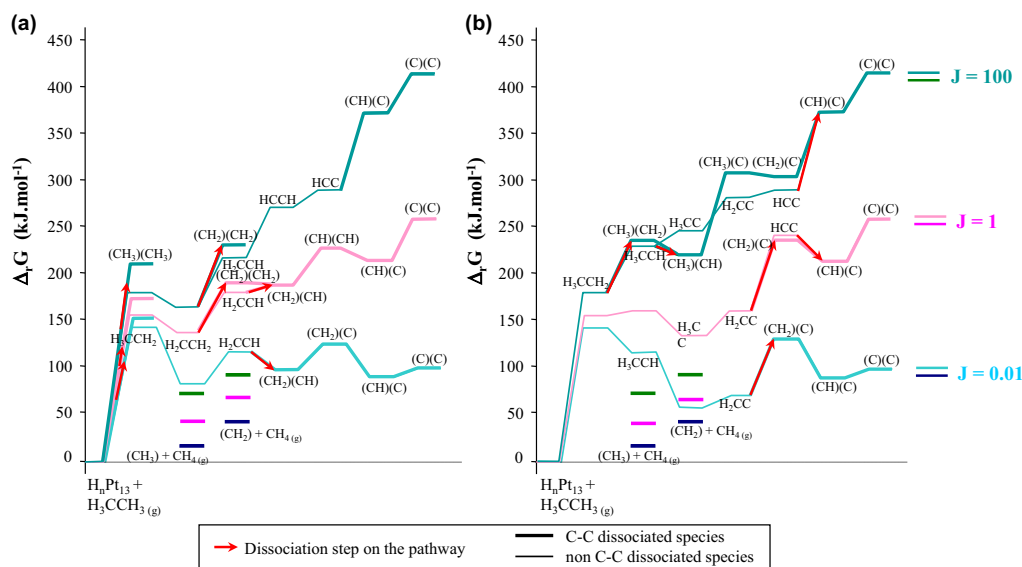


Fig. 6. $\Delta_r G$ profile of: (b) symmetric and (b) asymmetric dehydrogenation pathways, including intermediates issued from C–C bond scission when their formation is favorable, for $J = 0.01, 1$ and 100 . When two pathways are competitive, they are both shown. $J = 10$ was omitted for clarity. Parentheses delimit the monocarbonaceous species adsorbed on the cluster after the C–C bond breaking. Arrows represent some possible C–C bond scission pathways.

of an adsorbed C atom. The BP morphology can more easily accommodate such highly coordinated (C) species, but as it simultaneously involves a lower H content, the corresponding $\Delta_r G$ values become very high. Thus, the instability of coke and/or carbide precursors at $J = 100$ can also be assigned to morphology effects of the clusters.

5. Discussion

Understanding the effect of $P(H_2)$ on hydrogenolysis and dehydrogenation reactions is of paramount interest for the rational interpretation of experimental observations and beyond the optimization of the process conditions [1,2,13]. Regarding

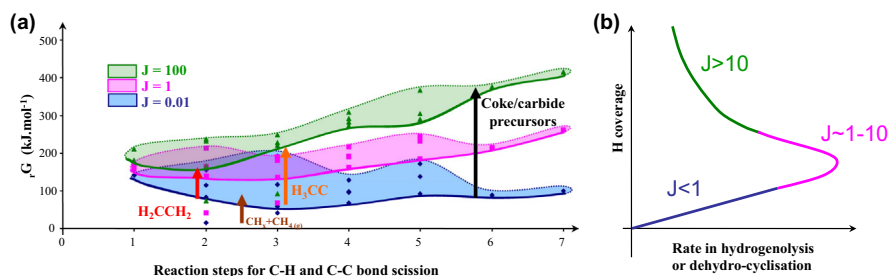


Fig. 7. (a) $\Delta_r G$ of all intermediates involved in dehydrogenation and/or C–C bond scission steps including hydrogenolysis for $J = 0.01, 1$ and 100 , respectively. Envelopes are drawn following the stability of each carbonaceous species: the blue ($J = 0.01$), pink ($J = 1$), and green ($J = 100$) envelopes encompass the carbonaceous species (except desorbed methane) for the corresponding J . Evolution of stability of key intermediates are highlighted by the red, brown, green, and black arrows for ethyl H_3CCH_2 , ethylene H_2CCH_2 , desorption of methane $\text{CH}_x + \text{CH}_4$ (g), ethynidyne H_3CC and coke/carbide precursors $[(\text{CH})(\text{C})$ and $(\text{C})(\text{C})$], respectively. The size of arrows is proportional to $\Delta_r G(J = 100) - \Delta_r G(0.01)$, corresponding to the thermodynamic sensitivity of adsorbed species as a function of reaction conditions. (b) Evolution of hydrogenolysis or dehydro-cyclization rate as a function of H coverage adapted from [85] for hydrogenolysis and from [2,14] for dehydrocyclization: the position of the maximum depends on the reactant and catalyst. (For interpretation of the references to color in this figure legend, the reader is referred to the web version of this article.)

hydrogenolysis first, it appears experimentally that ethane (as well as other alkanes) hydrogenolysis rate follows a volcano curve trend as a function of $P(\text{H}_2)$ [12] and of the H coverage on the metallic particles [85]. For the more complex dehydro-cyclization reaction targeted in the naphtha reforming process, a similar trend is also observed [1,2,14], which implies that the industrial process conditions must be carefully chosen with respect to the total and partial pressure of hydrogen mimicked by the parameter $J = P(\text{H}_2)/P(\text{C}_2\text{H}_6)$ in our thermodynamic model.

To our knowledge, previous theoretical studies investigating alkane activation on platinum have been done at zero hydrogen coverage either on ideal platinum surface [20–22] or on platinum cluster [23–25] and have not addressed this question.

As already shown in the absence of adsorbed hydrocarbon molecules [30], for high $P(\text{H}_2)$, the H/Pt ratio exceeds one and the morphology shifts from a biplanar to a cuboctahedral one (CUB). The results presented in this study highlight the impact of H content and of cluster morphology on the stability of adsorbed C_xH_y species ($x = 1$ or 2 and $0 \leq y \leq 5$) and reveal that CUB morphology can also be stabilized in the presence of C_xH_y species.

In order to further discuss the effect of hydrogen, Fig. 7a summarizes the evolution of thermodynamic stability of the various carbonaceous species as a function of J . The shape and position of the (blue–red–green) envelopes directly depend on J . Following the increase in H_2 partial pressure and thus the J value, the width of the envelopes varies from large (blue envelope) to narrow (green envelope). This reveals the narrowing of the interval of stability between the different intermediates when increasing $P(\text{H}_2)$. In other words, at low $P(\text{H}_2)$, and for a given reaction step, the system is thermodynamically more selective toward the formation of one well-defined intermediate. By contrast, high $P(\text{H}_2)$ induces a leveling of the stability of the different adsorbed intermediates at a given step. The lowest $\Delta_r G$ pathways (thick bottom lines of the envelopes) feature how the stable intermediates are sensitive to an increase in J . The vertical arrows feature this thermodynamic sensitivity of the key intermediates with respect to reaction conditions: the longer the arrow, the stronger the destabilization when J increases.

As illustrated by the black arrow, upon $P(\text{H}_2)$ increase highly dehydrogenated species such as acetylene (HCCH), $(\text{CH})(\text{C})$ and $(\text{C})(\text{C})$, are more rapidly destabilized than moderately dehydrogenated species: ethyl (H_3CCH_2), ethylene (H_2CCH_2), and ethynidyne (H_3CC). The highly dehydrogenated species, (HCCH), $(\text{CH})(\text{C})$ and $(\text{C})(\text{C})$, must be regarded either as coke precursors or as surface carbide precursors. For very low J values (e.g., 0.01), these species are thermodynamically close to ethylene and they may thus be at the origin of strong deactivation by coke or carbide formation mainly. In order to counterbalance this trend, one possibility is to change

the process conditions and to increase the partial pressure of H_2 . In particular, J values around or above 1 destabilize these highly dehydrogenated species (HCCH), $(\text{CH})(\text{C})$ and $(\text{C})(\text{C})$.

If we now focus on the comparison between dehydrogenation and hydrogenolysis, one should notice first that the formation of ethylene, for example, can be limited by the relatively poor stability of the ethyl species which formation is needed to reach ethylene. It is thus instructive to report the $\Delta_r G$ value of the less-stable intermediate encountered along the hydrogenolysis pathway leading to the $(\text{CH}_x)(\text{CH}_y)$ species, to elucidate potential thermodynamic limitations. This is done in Fig. 8, where the highest $\Delta_r G$ levels leading to the studied intermediate is plotted as a function of J . It is first shown that the dehydrogenation and hydrogenolysis are both destabilized by increasing J ; however, the hydrogenolysis profile is more rapidly destabilized than dehydrogenation particularly for $J \geq 10$. For very low J , as aforementioned, the C–C bond scission is competitive with dehydrogenation. In that case, hydrogenolysis involves dehydrogenated intermediate such as (H_3CCH) and (H_2CCH). Earlier experimental works [9–12] and more recent theoretical ones [25] proposed that alkane must lose a certain number of H atoms (probably more than 2) to help for the activation of the C–C bond. This is typically in line with our thermodynamic model where ethane, after losing 2 or 3 H atoms, forms (H_3CCH) and (H_2CCH) followed by C–C bond scission step at $J = 0.01$. At $J = 1$, the situation becomes more complex because the C–C bond scission would be thermodynamically more favorable on ethane leading to the formation of two methyl species. To our knowledge, this direct activation pathway was not reported in the literature so far and would require a deeper analysis on the kinetic aspects. By contrast, the $(\text{CH}_2)(\text{CH}_2)$ pathway is higher in

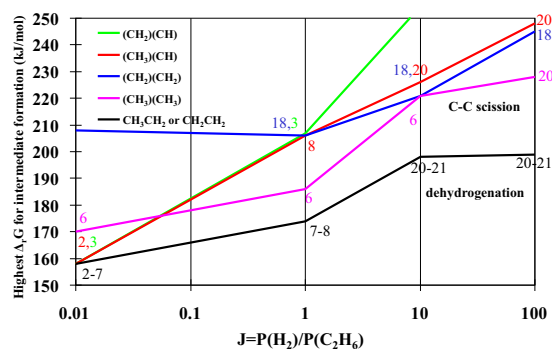


Fig. 8. Highest Gibbs free energy levels of intermediates involved in the formation of $(\text{CH}_x)(\text{CH}_y)$ species (C–C bond scission) and $(\text{CH}_3\text{CH}_2)(\text{CH}_2\text{CH}_2)$ species (dehydrogenation pathway). The number of hydrogen atoms co-adsorbed is reported.

energy by about 30 kJ mol^{-1} , but the Pt cluster exhibits a CUB morphology with much higher hydrogen (18) favoring statistically the close contact of two H atoms with CH_2 leading to methane. For $J = 10$, the C–C bond scission seems to be energetically competitive for three intermediates: $(\text{CH}_3)(\text{CH}_3)$, $(\text{CH}_2)(\text{CH}_2)$, and $(\text{CH}_3)(\text{CH})$. Here again, the number of hydrogen atoms co-adsorbed with $(\text{CH}_2)(\text{CH}_2)$ and $(\text{CH}_3)(\text{CH})$ is high. In that case, only the more highly dehydrogenated (H_2CCH) intermediate involved at low J seems to be ruled out.

Our thermodynamic analysis can also shed some light on the volcano curve observed experimentally for hydrogenolysis [12,85] and dehydrogenation reactions [1,2] when plotting their rates as a function of $P(\text{H}_2)$, as schematized in Fig. 7b). At low $P(\text{H}_2)$, the volcano curve exhibits an abrupt decreasing slope, which is rendered in our model by the strong impact of J and hydrogen coverage on the stability of highly dehydrogenated species precursor of coke and carbide (large black arrow in Fig. 7a). By contrast, at high $P(\text{H}_2)$, the decreasing slope of the volcano is smoother which also means that the sensitivity of dehydrogenation step to $P(\text{H}_2)$ is weaker (red and brown arrows). The three domains identified in [85] are reported in Fig. 7b) and correspond to different hydrogen coverages of the cluster as a function of the hydrogen pressure.

In the case of the dehydrogenation pathway, the nonzero partial pressure of hydrogen in the reaction medium is mandatory to avoid the formation of highly dehydrogenated carbonaceous compounds, acting as coke precursors and thus deactivating the catalyst. Let us extend this analysis to the case of naphtha reforming where the linear and cyclic alkanes are converted into aromatics through dehydro-cyclization mechanisms. To this end, the dehydrogenation step of alkanes into alkenes is at the core of the chemical process: either cyclo-alkanes are dehydrogenated into aromatics, or linear alkanes are dehydrogenated into alkenes before structural cyclization. This step is modeled by the “symmetric dehydrogenation” so-called and described above in the present work. The formation of the ethylene H_2CCH_2 species (as focused in the present study as a model compound) is thus of prior interest to understand the dehydrogenation activity of the metallic phase. Here again, an optimum in hydrogen pressure is industrially targeted to limit the formation of coke and loss of yield in dehydrogenation. As aforementioned, this is also true for the hydrogenolysis reaction, which is considered as an unwished side reaction in catalytic reforming. In addition, as it was underlined at the end of paragraph 4.3, we cannot overlook that the backwards rehydrogenation reaction may also take place upon increasing J . For J close to 10, due to the small thermodynamic barrier to rehydrogenate ethylene into an ethyl intermediate, this reverse process may become possible and thus decrease the hydrogenolysis and reforming rate. Thus, the optimal hydrogen partial pressure is a compromise between the energy cost of life cycle duration (coke and/or carbide deposit) and from the loss of yield mainly driven by the increase in energy levels (as reported in Fig. 8) of the targeted unsaturated products (aromatics or olefins) upon co-adsorbed hydrogen.

Our work also highlights the puzzling role of the ethylidyne intermediate which is formed from ethyl by dissymmetric dehydrogenation and may compete with ethylene formed by symmetric dehydrogenation. Moreover, in absence of $P(\text{H}_2)$, it was experimentally shown that ethylidyne is formed from ethylene itself [18,82–84]. According to our thermodynamic analysis (Fig. 4), the free energy minimum is shifted from ethylidyne H_3CC (at $J = 0.01$) to ethylene H_2CCH_2 (at $J = 10$): the transition being evaluated between $J = 1$ and 10. So using the optimal $P(\text{H}_2)$ is crucial in order to limit the formation of this unwished intermediate. Our results thus identify one key descriptor based on the relative stability of alkenes (ethylene H_2CCH_2 , in our study) versus alkylidyne (ethylidyne H_3CC) as a function of J . For $J = 1$, the $\Delta_r G$ of these two species are identical (Fig. 4a). Since alkylidyne can be considered as

dead end species located in an energy well along the unwished dissymmetric dehydrogenation pathway, it is mandatory to increase the hydrogen partial pressure (J between 1 and 10) to favor the preferential formation of ethylene in catalytic reforming conditions.

In industrial reforming processes using a pure Pt-based active phase, J is usually higher than 4 and $P(\text{H}_2)$ is comprised between 20–30 bars in order to increase the time between regenerations of the catalyst to the detriment of the yield. These optimal process conditions are consistent with the thermodynamic analysis reported before. To be able to use a lower $P(\text{H}_2)$, the alternative is to combine platinum with a second metallic element [86]. This element will play a role on the hydrogen coverage of the metallic particles as well as on the relative thermodynamic stability of intermediates. For instance, the destabilization of alkylidyne species as analyzed with DFT calculations on $\text{Pt}_3\text{Sn}(111)$ extended surface [70], unsupported $\text{Pt}_{16}\text{Sn}_9$ clusters [77], and experimental studies on PtSn/SiO_2 [77,79]. Considering the effect of the nature of the metal on hydrogenolysis itself, it is experimentally known that platinum is less active than other metals such as Os, Ru, Rh, Re, and Ir [87,88]. This might be attributed to two main intrinsic parameters. On the one hand, as also proposed in [85], the results of the present study locate platinum on the region of high H coverage of Fig. 7 b which may refrain dehydrogenation steps and enhance the backwards hydrogenation. This is also coherent with kinetic analyses giving an apparent order in $P(\text{H}_2)$ for hydrogenolysis, which is the most negative one in the platinum case [87,88]. The values obtained by the theoretical kinetic analysis are smaller (-1.7) than the observed one (-2.5) which leads the authors of Ref. [87] to suspect that “an additional effect is due to significant coverage of the surface by adsorbed hydrogen, not accounted in the simplified kinetic analysis.” On the other hand, the metal–carbon bond energy differs significantly from one metal to another. Referring to the DFT calculations by Toulhoat and Raybaud [89]—published 10 years earlier, for the 40th anniversary of Journal of Catalysis, the calculated Pt–C bond energy was lower than M–C bond energies calculated for $\text{M} = \text{Os}, \text{Ru}, \text{Rh}, \text{Re}, \text{and Ir}$. This trend certainly enhances the C–C bond activation required for hydrogenolysis catalyzed by these metals. So the nature of the metal will modify the H coverage by H and the nature of C_xH_y species inducing a displacement of the volcano maximum in Fig. 7b) for hydrogenolysis and dehydrogenation, as qualitatively discussed by Bond in Ref. [85].

6. Conclusions and perspectives

The recent progresses made in the DFT simulation of γ -alumina surfaces have allowed our community to tackle many challenging questions in heterogeneous catalysis. We have recalled some relevant but nonexhaustive examples where the Digne’s model published 10 years ago in Journal of Catalysis was used fruitfully: dehydration of alcohol, depollution of automotive exhausts, hydro-treatment, and hydrocracking. One important area of research has also concerned the description of γ -alumina-supported metallic particles with the application of reforming catalysts. In this case, we have proposed one advanced model of platinum nano-clusters supported on the γ -alumina (100) surface in reactive environment. It has been shown that this model which also included the effect of the (T, P) conditions can be used to furnish a rational explanation of the effect of hydrogen on the hydrogenolysis and dehydrogenation energy profiles.

For that purpose, structures and stabilities of adsorbed C_xH_y species ($x = 1$ or 2 and $0 \leq y \leq 5$) on $\gamma\text{-Al}_2\text{O}_3$ -supported Pt_{13} clusters for variable H coverage were investigated in the present work by DFT calculations including the effects of temperature and

pressure in the reactive medium. Calculated relative Gibbs free energy profiles for the transformation of ethane allowed the quantification of the relative stability of C_xH_y species relevant for dehydrogenation and hydrogenolysis pathways as a function of reaction conditions. The impact of the ratios of partial pressure of hydrogen over partial pressure of ethane ($J = 0.01, 1, 10$ and 100) have been studied on the following pathways:

- (i) moderate symmetric dehydrogenation (C–H bond scission) of ethane into valuable olefinic intermediates (namely ethylene),
- (ii) dissymmetric dehydrogenation (C–H bond scission) into dormant species (namely ethylidyne),
- (iii) C–C bond scission leading to coke precursors or surface carbide,
- (iv) C–C bond scission leading to hydrogenolysis.

According to the DFT and thermodynamic calculations, intermediate J values between 1 and 10 correspond to an optimal thermodynamic balance favoring dehydrogenation (i, ii) while avoiding the C–C bond scission leading to coke precursors or surface carbide (iii). Simultaneously, ethylidyne considered as a dead-end intermediate is thermodynamically less stable with respect to ethylene as soon as J becomes greater than 1. For high values of J , hydrogenolysis as well as dehydrogenation pathway are also expected to be thermodynamically hindered: the hydrogenolysis route being more affected due to the stronger destabilization of monocarbonaceous species on the cluster at high $P(H_2)$.

As a consequence, our DFT study quantified the interval of process conditions to be used for favoring moderate dehydrogenation of alkanes into olefins. It also gives a rational explanation of the thermodynamic optima in hydrogen pressure for maximizing either dehydrogenation or hydrogenolysis and avoiding coke formation catalyzed by platinum clusters highly dispersed on γ -alumina. The respective positions of the optima in hydrogenolysis and dehydrogenation result from a subtle thermodynamic balance between the stability of the key carbonaceous intermediates involved in both reactions and hydrogen coverages. We also proposed perspectives on the possible impacts of the addition of a second element (such as Sn) to platinum: this will be the scope of further deeper investigations based on recently established DFT models for PtSn clusters supported on γ -alumina [86].

Further kinetic investigations and transition state calculations are needed for a deeper understanding of mechanisms although the present thermodynamic considerations already provide relevant insights for a better control of reaction conditions during the catalytic process. In addition, increasing the size of the studied molecule will be relevant in the future to go further in the understanding of the reactions involved in catalytic reforming conditions.

Acknowledgments

All calculations were performed at IFPEN HPC center and at IDRIS/CINES HPC centers within projects x2010086134 and x2011086134 funded by GENCI.

Appendix A. Supplementary material

Supplementary data associated with this article can be found, in the online version, at <http://dx.doi.org/10.1016/j.jcat.2013.08.015>.

References

- [1] J.H. Sinfelt, Catalytic reforming, in: G. Ertl, E. Knözinger, J. Weitkamp (Eds.), *Handbook of Heterogeneous Catalysis*, Wiley, Weinheim, 1997, pp. 1939–1955.
- [2] J.P. Franck, in: B. Imelik, G.A. Martin, A.J. Renouprez (Eds.), *Fundamental and Industrial Aspects of Catalysis by Metals*, Editions du CNRS, Paris, 1984, p. 412.
- [3] Y. Barron, D. Cornet, G. Maire, F.G. Gault, J. Catal. 2 (1963) 152–155.
- [4] J.R. Anderson, R.J. Macdonald, Y. Shimoyama, J. Catal. 20 (1971) 147–162.
- [5] J.M. Muller, F.G. Gault, J. Catal. 24 (1972) 361–364.
- [6] J.A. Labinger, J.E. Bercaw, Nature 417 (2002) 507–514.
- [7] S. Vajda, M.J. Pellin, J.P. Greeley, C.L. Marshall, L.A. Curtiss, G.E. Ballentine, J.M. Elam, S. Catillon-Mucherie, P.C. Redfern, F. Mehmood, P. Zapol, Nat. Mater. 8 (2009) 213–216.
- [8] E. McFarland, Science 338 (2012) 340.
- [9] J.H. Sinfelt, Catal. Rev. 3 (1970) 175–205.
- [10] J.H. Sinfelt, J. Catal. 27 (1972) 468–471.
- [11] J.H. Sinfelt, Adv. Catal. 23 (1973) 91–119.
- [12] G.C. Bond, R.H. Cunningham, J. Catal. 166 (1997) 172–185.
- [13] G.C. Bond, *Metal-Catalyzed Reactions of Hydrocarbons*, Springer, New York, 2005.
- [14] G. Abolhamd, IFP Thesis, 1980.
- [15] L.L. Kesmodel, L.H. Dubois, G.A. Somorjai, J. Chem. Phys. 70 (1979) 2180–2188.
- [16] Y.Y. Yeo, A. Stuck, C.E. Wartnaby, D.A. King, Chem. Phys. Lett. 259 (1996) 28–36.
- [17] J.J.W. Harris, V. Fiorin, C.T. Campbell, D.A. King, J. Phys. Chem. B 109 (2005) 4069–4075.
- [18] S.M. Davis, F. Zaera, G.A. Somorjai, J. Am. Chem. Soc. 104 (1982) 7453–7461.
- [19] M. Santhosh Kumar, D. Chen, J.C. Walmsley, A. Holmen, Catal. Commun. 9 (2008) 747–750.
- [20] Y. Chen, D.G. Vlachos, J. Phys. Chem. C 114 (2010) 4973–4982.
- [21] H.A. Aleksandrov, L.V. Moskalova, Z.-J. Zhao, D. Basaran, Z.-X. Chen, D. Mei, N. Rösch, J. Catal. 285 (2012) 187–195.
- [22] Z.J. Zhao, L.V. Moskalova, H.A. Aleksandrov, D. Basaran, N. Rösch, J. Phys. Chem. C 114 (2010) 12190–12201.
- [23] J. Kua, W.A. Goddard, J. Phys. Chem. B 102 (1998) 9492–9500; J. Kua, W.A. Goddard, J. Phys. Chem. B 103 (1999) 2318.
- [24] R.M. Watwe, B.E. Spiewak, R.D. Cortright, J.A. Dumesic, J. Catal. 180 (1998) 184–193.
- [25] R.M. Watwe, R.D. Cortright, J.K. Nørskov, J.A. Dumesic, J. Phys. Chem. B 104 (2000) 2299–2310.
- [26] G.P. Petrova, G.N. Vayssilov, N. Rosch, Catal. Sci. Technol. 1 (2011) 958–970.
- [27] C. Chizallet, G. Bonnard, E. Krebs, L. Bisson, C. Thomazeau, P. Raybaud, J. Phys. Chem. C 115 (2011) 12135–12149.
- [28] C.H. Hu, C. Chizallet, C. Mager-Maury, M. Corral Valero, P. Sautet, H. Toulhoat, P. Raybaud, J. Catal. 274 (2010) 99–110.
- [29] C.H. Hu, C. Chizallet, H. Toulhoat, P. Raybaud, Phys. Rev. B 79 (195416) (2009) 195411.
- [30] C. Mager-Maury, G. Bonnard, C. Chizallet, P. Sautet, P. Raybaud, ChemCatChem 3 (2011) 200–207.
- [31] M. Digne, P. Sautet, P. Raybaud, P. Euzen, H. Toulhoat, J. Catal. 211 (2002) 1–5.
- [32] M. Digne, P. Sautet, P. Raybaud, P. Euzen, H. Toulhoat, J. Catal. 226 (2004) 54–68.
- [33] X. Krokidis, P. Raybaud, A.E. Gobichon, B. Rebours, P. Euzen, H. Toulhoat, J. Phys. Chem. B 105 (2001) 5121–5130.
- [34] H. Knözinger, P. Ratnasamy, Catal. Rev. 17 (1978) 31–70.
- [35] R.H.R. Castro, D.V. Quach, J. Phys. Chem. C 116 (2012) 24726–24733.
- [36] J.H. Kwak, R. Rousseau, D. Mei, C.H.F. Peden, J. Szanyi, ChemCatChem 3 (2011) 1557–1561.
- [37] J. Kwak, D. Mei, C.F. Peden, R. Rousseau, J. Szanyi, Catal. Lett. 141 (2011) 649–655.
- [38] J.H. Kwak, J. Hu, D. Mei, C.W. Yi, D.H. Kim, C.H.F. Peden, L.F. Allard, J. Szanyi, Science 325 (2009) 1670–1673.
- [39] J. Joubert, A. Salameh, V. Krakoviack, F. Delbecq, P. Sautet, C. Copéret, J.M. Basset, J. Phys. Chem. B 110 (2006) 23944–23950.
- [40] R. Wischert, P. Laurent, C. Copéret, F. Delbecq, P. Sautet, J. Am. Chem. Soc. 134 (2012) 14430–14449.
- [41] R. Wischert, C. Copéret, F. Delbecq, P. Sautet, Chem. Commun. 47 (2011) 4890–4892.
- [42] P. Sautet, F. Delbecq, Chem. Rev. 110 (2009) 1788–1806.
- [43] A. Salameh, J. Joubert, A. Baudouin, W. Lukens, F. Delbecq, P. Sautet, J.M. Basset, C. Copéret, Angew. Chem., Int. Ed. 46 (2007) 3870–3873.
- [44] M. Delgado, C.C. Santini, F. Delbecq, A. Baudouin, A. De Mallmann, C. Prestipino, S. Norsic, P. Sautet, J.-M. Basset, J. Phys. Chem. C 115 (2011) 6757–6763.
- [45] A. Motta, I.L. Fragalà, T.J. Marks, J. Am. Chem. Soc. 130 (2008) 16533–16546.
- [46] L.A. Williams, N. Guo, A. Motta, M. Delferro, I.L. Fragalà, J.T. Miller, T.J. Marks, PNAS 110 (2013) 413–418.
- [47] D. Mei, Q. Ge, J.H. Kwak, D.H. Kim, J.n. Szanyi, C.H.F. Peden, J. Phys. Chem. C 112 (2008) 18050–18060.
- [48] J.H. Kwak, D. Mei, C.-W. Yi, D.H. Kim, C.H.F. Peden, L.F. Allard, J. Szanyi, J. Catal. 261 (2009) 17–22.
- [49] C. Chizallet, P. Raybaud, Angew. Chem., Int. Ed. 48 (2009) 2891–2893.
- [50] C. Chizallet, P. Raybaud, ChemPhysChem 11 (2010) 105–108.

- [51] F. Leydier, C. Chizallet, A. Chaumonnot, M. Digne, E. Soyer, A.A. Quoineaud, D. Costa, P. Raybaud, *J. Catal.* 284 (2011) 215–229.
- [52] F. Leydier, C. Chizallet, D. Costa, P. Raybaud, *Chem. Commun.* 48 (2012) 4076–4078.
- [53] C. Arrouvel, M. Breyse, H. Toulhoat, P. Raybaud, *J. Catal.* 232 (2005) 161–178.
- [54] D. Costa, C. Arrouvel, M. Breyse, H. Toulhoat, P. Raybaud, *J. Catal.* 246 (2007) 325–343.
- [55] M. Digne, P. Raybaud, P. Sautet, D. Guillaume, H. Toulhoat, *J. Am. Chem. Soc.* 130 (2008) 11030–11039.
- [56] C. Mager-Maury, C. Chizallet, P. Sautet, P. Raybaud, *ACS Catal.* 2 (2012) 1346–1357.
- [57] B.J. Kip, F.B.M. Duivenvoorden, D.C. Koningsberger, R. Prins, *J. Catal.* 105 (1987) 26–38.
- [58] E. Bus, J.A. van Bokhoven, *Phys. Chem. Chem. Phys.* 9 (2007) 2894–2902.
- [59] F. Behafarid, L.K. Ono, S. Mostafa, J.R. Croy, G. Shafai, S. Hong, T.S. Rahman, S.R. Bare, B. Roldan Cuenya, *Phys. Chem. Chem. Phys.* 14 (2012) 11766–11779.
- [60] P. Raybaud, C. Chizallet, H. Toulhoat, P. Sautet, *Phys. Chem. Chem. Phys.* 14 (2012) 16773–16774.
- [61] J. Perdew, Y. Wang, *Phys. Rev. B* 45 (1992) 13244–13249.
- [62] G. Kresse, J. Hafner, *Phys. Rev. B* 49 (1994) 14251–14269.
- [63] G. Kresse, J. Furthmüller, *Comput. Mater. Sci.* 6 (1996) 15–50.
- [64] G. Kresse, D. Joubert, *Phys. Rev. B* 59 (1999) 1758–1775.
- [65] DMol3 is Accessible through the Materials Studio 6.0 Interface Commercialized by Accelrys Inc.
- [66] F. Mittendorfer, C. Thomazeau, P. Raybaud, H. Toulhoat, *J. Phys. Chem. B* 107 (2003) 12287–12295.
- [67] J.M. Essen, J. Haubrich, C. Becker, K. Wandelt, *Surf. Sci.* 601 (2007) 3472–3480.
- [68] R. Hirschl, A. Eichler, J. Hafner, *J. Catal.* 226 (2004) 273–282.
- [69] G.W. Watson, R.P.K. Wells, D.J. Willock, G.J. Hutchings, *J. Phys. Chem. B* 104 (2000) 6439–6446.
- [70] R.M. Watwe, R.D. Cortright, M. Mavrikakis, J.K. Norskov, J.A. Dumesic, *J. Chem. Phys.* 114 (2001) 4663–4668.
- [71] Q. Ge, D.A. King, *J. Chem. Phys.* 110 (1999) 4699–4702.
- [72] S.G. Podkolzin, R. Alcalá, J.A. Dumesic, *J. Mol. Catal. A* 218 (2004) 217–227.
- [73] V. Nieminen, K. Honkala, A. Taskinen, D.Y. Murzin, *J. Phys. Chem. C* 112 (2008) 6822–6831.
- [74] J.F. Paul, P. Sautet, *J. Phys. Chem.* 98 (1994) 10906–10912.
- [75] B. Hammer, J.K. Nørskov, *Adv. Catal.* 45 (2000) 71–129.
- [76] F. Zaera, D. Chrysostomou, *Surf. Sci.* 457 (2000) 71–88.
- [77] J. Shen, J.M. Hill, R.M. Watwe, B.E. Spiewak, J.A. Dumesic, *J. Phys. Chem. B* 103 (1999) 3923–3934.
- [78] B.E. Spiewak, R.D. Cortright, J.A. Dumesic, *J. Catal.* 176 (1998) 405–414.
- [79] R.D. Cortright, J.A. Dumesic, *J. Catal.* 148 (1994) 771–778.
- [80] P.D. Ditlevsen, M.A. Van Hove, G.A. Somorjai, *Surf. Sci.* 292 (1993) 267–275.
- [81] A.T. Anghel, S.J. Jenkins, D.J. Wales, D.A. King, *J. Phys. Chem. B* 110 (2006) 4147–4156.
- [82] F. Zaera, C.R. French, *J. Am. Chem. Soc.* 121 (1999) 2236–2243.
- [83] R. Deng, E. Herceg, M. Trenary, *J. Am. Chem. Soc.* 127 (2005) 17628–17633.
- [84] R.D. Cortright, R.M. Watwe, J.A. Dumesic, *J. Mol. Catal. A* 163 (2000) 91–103.
- [85] G.C. Bond, *Catal. Today* 49 (1999) 41–48.
- [86] A. Jahel, V. Moizan-Baslé, C. Chizallet, P. Raybaud, J. Olivier-Fourcade, J.C. Jumas, P. Avenier, S. Lacombe, *J. Phys. Chem. C* 116 (2012) 10073–10083.
- [87] J.H. Sinfelt, D.J.C. Yates, *J. Catal.* 8 (1967) 82–90.
- [88] J.H. Sinfelt, *Catal. Lett.* 9 (1991) 159–171.
- [89] H. Toulhoat, P. Raybaud, *J. Catal.* 216 (2003) 63–72.